Numerical investigation on particle inertial migration in circular Poiseuille flow with thermal convection

Jingwen Fu, Wenwei Liu,* Xing Jin, and Yun Huang
State Key Laboratory of Mesoscience and Engineering, Institute of Process Engineering, Chinese Academy of Sciences, Beijing 100190, China
and School of Chemical Engineering, University of Chinese Academy of Sciences, Beijing 100049, China

(Received 5 February 2024; accepted 14 May 2024; published 7 June 2024)

In this work, a numerical study on the inertial migration of particle suspension in a circular pipe with thermal effect is performed by means of the lattice Boltzmann method and the discrete element method. Both constant temperature and varied temperature conditions are taken into consideration. The migration behavior and the heat transfer are well characterized in terms of the circumferential and radial positions as well as the Nusselt number. The results show that particles tend to migrate toward the pipe bottom due to the thermal buoyancy when the fluid's temperature is higher than the particle's. For a single particle with constant temperature, it is shown that the variation of circumferential equilibrium position can be well regressed by the Richardson number and divided into three zones, i.e., an inertial lift dominating zone, a transition zone, and a buoyancy dominating zone. Both the radial equilibrium position and the Nusselt number are sensitive to the Reynolds number and increase consistently with the Grashof number. For particle suspension with constant temperature, similar migration behavior is observed with an enlarged transition zone. However, a nonmonotonic variation of the radial equilibrium position as well as the Nusselt number is discovered, which is attributed to the particle crowding effect. For varied temperature conditions, the migration process is affected by the heat capacity ratio and the Prandtl number, which determine the heating rate of the particle. Nevertheless, the radial equilibrium position is irrelevant with the thermal effect, which only depends on the Reynolds number and resembles the isothermal condition.

DOI: 10.1103/PhysRevFluids.9.064302

I. INTRODUCTION

Particle transport in Poiseuille flow is a classic subject in the investigation of multiphase flow and holds significant importance in engineering applications [1,2]. Particle inertial migration is an interesting phenomenon that was first discovered by Segré and Silberberg [3] in 1961. It was found that randomly distributed particles migrate toward a specific equilibrium position between the centerline and the wall of the channel or pipe. For particle-laden flow in a circular pipe, inertial migration leads to the formation of a particle annulus close to the wall, while particles migrate to four points near the middle of the wall in a square channel [4]. Currently, due to the applications in microfluid for particle mixing, sorting, and capturing, particle inertial migration has been widely investigated [5–8].

Numerous studies have been conducted through theoretical analyses, experiments, and numerical simulations to investigate the particle inertial migration process. Theoretically, a singular perturbation expansion method [9] and matched asymptotic expansion [10,11] have been adopted to

*liuwenwei@ipe.ac.cn

 ©2024 American Physical Society

predict the equilibrium position of particle inertial migration. Experimentally, it was found by Han *et al.* [12] that the particle migration process is significantly influenced by the Reynolds number and solid volume fraction of suspension. Matas *et al.* [13] conducted experiments with various particle sizes, and the results aligned with theoretical analysis employing matched asymptotic expansion. Additionally, Di Carlo *et al.* [14] discussed the finite size effect of particles and the lift force through experimental and numerical approaches. Numerically, the fictitious domain method [15] and the lattice Boltzmann method (LBM) [16–18] have been employed to investigate the migration mechanism and particle equilibrium positions. Recently, the inertial migration of nonspherical particles was investigated in several studies [19–21], revealing that the streamwise particle velocity and migration velocity are affected by particle shapes due to the difference in particle rotation. Furthermore, for migration involving deformable particles, damped oscillations [22] and a faster velocity for particles around the channel center [23] are observed. In the case of migration involving a deformable biconcave capsule, as a representation of a red blood cell, the equilibrium particle position is influenced by the bistable flow modes, i.e., the rolling and tumbling motion [24].

Particle migration behavior is influenced while introducing additional effects [25–29], where thermal effect is one of the most important factors for particle-laden flow [30–34]. Thermal buoyancy, originating from thermal convection, is a key factor influencing particle movement. Currently, numerous investigations focusing on the effect of thermal convection in the particle settling process have been carried out. For instance, when a cold particle settles in a hot fluid, the particle migrates toward the wall or oscillates laterally with the increase of the Grashof number [35,36]. The well-known draft-kissing-tumbling (DKT) process for a pair of particles is also influenced by the thermal effect, leading to particle separation for cold particles and aggregation for hot particles [37]. For two settling particles, it was observed by Yang [38] that the DKT phenomenon occurs earlier and the oscillations of particle trajectories are enhanced due to thermal convection. Additionally, Hashemi *et al.* [39] investigated the settling process of a group of hot particles, revealing that the settling velocity is reduced due to the effect of the thermal buoyancy and the development of asymmetric vortex shedding compared with the isothermal single particle condition.

Undoubtedly, the thermal convection resulting from the temperature gradient between the particles and the fluid makes a big difference compared with the isothermal condition, especially for the microfluidic applications. However, to the best of our knowledge, limited attention has been paid to such kind of study. Hu and Guo [40] numerically studied the effect of thermal convection on particle migration in a two-dimensional (2D) Poiseuille flow. A notable discovery was that the symmetric equilibrium positions about the centerline converge to a single equilibrium position below the channel center when the Grashof number reaches a critical value. This phenomenon was further investigated by Liu and Wu [41], who found that the critical Grashof number, beyond which a lateral equilibrium position shift occurs, is dependent on the Reynolds number and the particle-to-channel size ratio. Additional studies involve numerical investigations on the particle migration in simple shear flow with thermal fluids [42,43].

However, previous studies on inertial migration in thermal fluids are insufficient due to the following limitations. Firstly, most studies are confined to 2D cases and focus only on single-particle behavior, which deviates from realistic applications where particle suspensions are commonly encountered. Secondly, the temperature difference between the particle and the fluid is assumed to be constant in most studies, which is short of a physics foundation. In practice, it is expected that the dynamic migration behavior should be strongly related to the temperature evolution of both the particle and the fluid. Nevertheless, very few studies considering these factors comprehensively can be found in the existing literature.

In this work, the lattice Boltzmann method (LBM) coupled with the discrete element method (DEM) was employed to numerically investigate the particle inertial migration in a three-dimensional circular pipe in the presence of thermal convection. The migration behavior as well as the heat transfer of both single-particle and dilute suspensions with constant and varied temperature

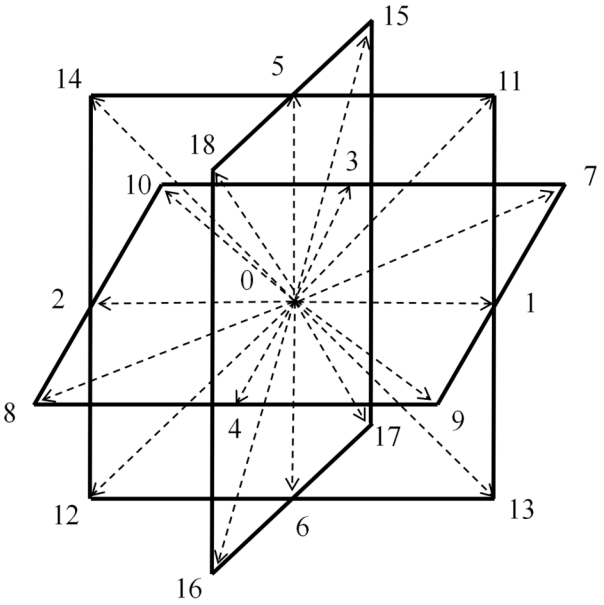

FIG. 1. Directions of discrete velocity in the D3Q19 model.

are investigated. The current work is organized as follows. The numerical method is described in Sec. II. The physical model and the validation tests are introduced in Sec. III. Section IV gives the detailed results and discussion, and the conclusions are drawn in Sec. V.

II. NUMERICAL METHOD

A. Lattice Boltzmann method

In this work, a double-population lattice Boltzmann method with a single relaxation time model is adopted [44,45]. The governing equations are expressed as follows [46]:

$$f_i(\mathbf{x}+\mathbf{e}_i\Delta t, t+\Delta t) - f_i(\mathbf{x},t) = -\frac{\Delta t}{\tau_f}\left[f_i(\mathbf{x},t) - f_i^{\mathrm{eq}}(\mathbf{x},t)\right] + F_i\Delta t, \tag{1}$$

$$g_i(\mathbf{x}+\mathbf{e}_i\Delta t, t+\Delta t) - g_i(\mathbf{x},t) = -\frac{\Delta t}{\tau_g}\left[g_i(\mathbf{x},t) - g_i^{\mathrm{eq}}(\mathbf{x},t)\right] + S_i\Delta t, \tag{2}$$

where $f_i(\mathbf{x},t)$ is the distribution function of fluid and $g_i(\mathbf{x},t)$ is the distribution function of temperature. F_i and S_i are the external body force and heat source terms, respectively. In this work, no external heat source is considered, so S_i is ignored. Δt is the time step. τ_f and τ_g are the relaxation times for fluid and temperature, respectively. $\mathbf{e}_i$ is the discrete velocity, as shown in Fig. 1.

The equilibrium distribution functions are expressed as

$$f_i^{\mathrm{eq}} = \rho\omega_i\left[1 + \frac{\mathbf{e}_i\cdot\mathbf{u}}{c_s^2} + \frac{(\mathbf{e}_i\cdot\mathbf{u})^2}{2c_s^4} - \frac{u^2}{2c_s^2}\right], \tag{3}$$

$$g_i^{\mathrm{eq}} = T\omega_i\left[1 + \frac{\mathbf{e}_i\cdot\mathbf{u}}{c_s^2}\right], \tag{4}$$

in which c_s is the lattice sound speed and is equal to $1/\sqrt{3}$, and ω_i is the weight coefficient where $\omega_0 = 1/3$, $\omega_{1,\ldots,6} = 1/18$, and $\omega_{7,\ldots,18} = 1/36$. The macroscopic fluid density ρ, temperature T, and the fluid velocity $\mathbf{u}$ are obtained based on the distribution function,

$$\rho = \sum_i f_i, \tag{5}$$

$$\rho\mathbf{u} = \sum_i f_i\mathbf{e}_i + \frac{\Delta t}{2}\mathbf{F}, \tag{6}$$

$$T = \sum_i g_i, \tag{7}$$

where $\mathbf{F}$ is the macroscopic body force. The external body force in Eq. (1) is determined following Guo's force scheme [47],

$$F_i = \left(1 - \frac{1}{2\tau_f}\right)\omega_i\left[\frac{\mathbf{e}_i - \mathbf{u}}{c_s^2} + \frac{\mathbf{e}_i \cdot \mathbf{u}}{c_s^4}\mathbf{e}_i\right] \cdot \mathbf{F}. \tag{8}$$

In order to couple the flow field and the temperature field, the Boussinesq approximation is adopted as

$$\rho = \rho_0[1 - \beta(T - T_{\text{ref}})], \tag{9}$$

where ρ_0 is the fluid density at the reference temperature T_{ref} and β is the fluid thermal expansion coefficient. The fluid buoyancy force originated from temperature difference and its magnitude per unit volume is defined as

$$\mathbf{F}_B = -\rho_0\mathbf{g}\beta(T - T_{\text{ref}}), \tag{10}$$

where $\mathbf{g}$ is the gravitational acceleration. By employing the Chapman-Enskog multiscale expansion, the microscopic lattice Boltzmann equation can recover to the macroscopic governing equations for mass, momentum, and energy transport, which can be written as follows:

$$\frac{\partial\rho}{\partial t} + \nabla \cdot (\rho\mathbf{u}) = 0, \tag{11}$$

$$\rho\frac{\partial\mathbf{u}}{\partial t} + \rho(\mathbf{u} \cdot \nabla)\mathbf{u} = -\nabla p + \mu\nabla^2\mathbf{u} + \mathbf{F}, \tag{12}$$

$$\frac{\partial T}{\partial t} + \nabla \cdot (T\mathbf{u}) = \nabla \cdot (\alpha\nabla T), \tag{13}$$

where μ is the fluid dynamic viscosity and α is the thermal diffusion coefficient. p is the fluid pressure and is determined by

$$p = c_s^2\rho. \tag{14}$$

Through Chapman-Enskog expansion the fluid kinematic viscosity and the thermal diffusion coefficient are related to the relaxation parameters,

$$\nu_f = c_s^2\left(\tau_f - \frac{\Delta t}{2}\right), \tag{15}$$

$$\alpha = c_s^2\left(\tau_g - \frac{\Delta t}{2}\right). \tag{16}$$

B. Fluid-solid coupling

In this work, a modified bounce-back scheme with second-order accuracy is adopted [48,49]. When simulating the movement of a solid particle within a fluid domain, the solid boundary of the particle is typically not precisely positioned on any lattice node. Assume that the solid boundary lies

between a fluid node $\boldsymbol{x}_f$ and a solid node $\boldsymbol{x}_s$ at time t, and the exact position of the solid boundary is defined as $\boldsymbol{x}_b$. The relative location of the solid boundary is described with a weighting parameter, q, which is defined as

$$q = \frac{|\boldsymbol{x}_f - \boldsymbol{x}_b|}{|\boldsymbol{x}_f - \boldsymbol{x}_s|}. \tag{17}$$

The distribution function at the boundary is calculated with first-order interpolation,

$$f_i(\mathbf{x}_b, t + \Delta t) = q f_i(\mathbf{x}_f, t) + (1 - q) f_i(\mathbf{x}_{ff}, t), \tag{18}$$

where $f_i(\mathbf{x}_f, t)$ and $f_i(\mathbf{x}_{ff}, t)$ are the existing distribution functions at the node $\mathbf{x}_f$ and the nearest node $\mathbf{x}_{ff}$, respectively. Then, a bounce-back operation is performed at the solid boundary instantaneously,

$$f_{-i}(\mathbf{x}_b, t + \Delta t) = f_i(\mathbf{x}_b, t + \Delta t) - 2\omega_i \rho \frac{\mathbf{u}_b \cdot \mathbf{e}_i}{c_s^2}, \tag{19}$$

where $\mathbf{u}_b$ is the velocity of the solid boundary and $\mathbf{e}_i$ the points from the fluid to the solid. Finally, the undetermined distribution function $f_{-i}(\mathbf{x}_f, t + \Delta t)$ is calculated by the first-order interpolation with the new $f_{-i}(\mathbf{x}_b, t + \Delta t)$ and the existing distribution function $f_{-i}(\mathbf{x}_{ff}, t + \Delta t)$ as

$$f_{-i}(\mathbf{x}_f, t + \Delta t) = \frac{1}{1+q} f_{-i}(\mathbf{x}_b, t + \Delta t) + \frac{q}{1+q} f_{-i}(\mathbf{x}_{ff}, t + \Delta t). \tag{20}$$

In order to reduce the numerical error in calculation, the momentum exchanging method with Galilean invariance is employed [48]. The hydrodynamic force and torque at the solid boundary are evaluated with total momentum exchange, by summing up all the contributions from every lattice direction and the node near the solid boundary:

$$\mathbf{F}_f = \sum_{\text{all } x_f} \sum_i [(\mathbf{e}_i - \mathbf{u}_b) f_i^+(\mathbf{x}_f, t) - (\mathbf{e}_{-i} - \mathbf{u}_b) f_{-i}(\mathbf{x}_f, t + \Delta t)], \tag{21}$$

$$\mathbf{M}_f = \sum_{\text{all } x_f} \sum_i (x_b - x_c) \times [(\mathbf{e}_i - \mathbf{u}_b) f_i^+(\mathbf{x}_f, t) - (\mathbf{e}_{-i} - \mathbf{u}_b) f_{-i}(\mathbf{x}_f, t + \Delta t)]. \tag{22}$$

In the above equations, $f_i^+(\mathbf{x}_f, t)$ is the post-collision distribution function, $f_{-i}(\mathbf{x}_f, t + \Delta t)$ is the bounced-back distribution function from the solid boundary calculated with Eq. (20), and x_c is the position of the particle center. In terms of temperature boundary condition, the Dirichlet boundary condition is adopted for all calculations in this work. A general bounce-back scheme for the concentration boundary is employed, and the undetermined temperature distribution function is given as follows [50]:

$$g_{-i}(\mathbf{x}_f, t + \Delta t) = -g_i^+(\mathbf{x}_f, t) + 2\omega_i T_b \times [1.0 + 4.5(\mathbf{e}_i \cdot \mathbf{u}_b)^2 - 1.5|\mathbf{u}_b|^2], \tag{23}$$

in which T_b is the temperature at the boundary while $-g_i^+(\mathbf{x}_f, t)$ is the post-collision distribution function.

C. Discrete element method

The soft sphere model is adopted in the current work, and the particle can translate and rotate freely in the computational domain according to Newton's second law,

$$m \frac{d\mathbf{U}_p}{dt} = \mathbf{F}_f + \mathbf{F}_c, \tag{24}$$

$$I \frac{d\boldsymbol{\Omega}_p}{dt} = \mathbf{M}_f + \mathbf{M}_c, \tag{25}$$

where $\mathbf{U}_p$ is the particle translational velocity, $\boldsymbol{\Omega}_p$ is the rotational velocity, m is the particle mass, and I is the moment of inertia. $\mathbf{F}_f$ and $\mathbf{M}_f$ are the force and torque exerted on the particle from the

fluid, respectively. It should be noted that the fluid lubrication force is not considered in the current work, as the wet collision mechanism is not completely understood so far [51] and it is still very tricky to deal with the discrete element method and the lubrication model at the same time.

$\mathbf{F}_c$ and $\mathbf{M}_c$ are the force and torque exerted on the particle from particle-particle contact, respectively. $\mathbf{F}_c$ and $\mathbf{M}_c$ can be expressed as

$$\mathbf{F}_c = F_n\mathbf{n} + F_s\mathbf{t}_s, \tag{26}$$

$$\mathbf{M}_c = \frac{dF_s(\mathbf{n}\times\mathbf{t}_s)}{2} + M_r(\mathbf{t}_R\times\mathbf{n}) + M_t\mathbf{n}, \tag{27}$$

where d is the particle diameter, F_n is the normal force, F_s is the tangential force, M_r is the rolling resistance, and M_t is the twisting resistance. $\mathbf{n}$, $\mathbf{t}_s$, and $\mathbf{t}_R$ are the unit vectors of the normal force, tangential force, and rolling direction, respectively.

The normal force is described by the Hertz model considering the influence of damping and is expressed as

$$F_n = -k_n\delta_n^{1.5} - \eta_n\mathbf{v}_r\cdot\mathbf{n}, \tag{28}$$

where η_n is the normal dissipation coefficient and $\mathbf{v}_r$ is the relative velocity at the contact point. δ_n is the overlap at the normal direction and it is defined as $\delta_n = r_{p,i} + r_{p,j} - |x_j - x_i|$ for particles with radius r_p and position x. k_n is the normal stiffness and it is defined as

$$k_n = \frac{4}{3}E\sqrt{R}, \tag{29}$$

$$\frac{1}{R} = \frac{1}{r_{p,i}} + \frac{1}{r_{p,j}}, \tag{30}$$

$$\frac{1}{E} = \frac{1-\nu_i^2}{E_i} + \frac{1-\nu_j^2}{E_j}, \tag{31}$$

where E and R are the effective elastic moduli and radius, respectively. ν is the Poisson's ratio. The sliding model is adopted as

$$F_s = -k_T\xi_T - \eta_T\mathbf{v}_s\cdot\mathbf{t}_s, \tag{32}$$

where k_T is the spring stiffness coefficient in the tangential direction, $\mathbf{v}_s$ is the relative sliding velocity, and η_T is the sliding dissipation coefficient. $\xi_T = \int_{t_0}^{t}\mathbf{v}_s(t)\cdot\mathbf{t}_s dt$ is the tangential displacement. The rolling model is given as

$$M_r = -k_R\xi_R - \eta_R\mathbf{v}_L\cdot\mathbf{t}_R, \tag{33}$$

where $\mathbf{v}_L = -R(\boldsymbol{\Omega}_i - \boldsymbol{\Omega}_j)\times\mathbf{n}$ is the rolling velocity, $\mathbf{t}_R = \mathbf{v}_L/|\mathbf{v}_L|$ is the rolling direction, $\xi_R = \int_{t_0}^{t}\mathbf{v}_L(t)\cdot\mathbf{t}_R dt$ is the rolling displacement, k_R is the rolling stiffness, and η_R is the rolling damping coefficient. The twisting model is given as

$$M_t = -k_Q\xi_Q - \eta_Q\Omega_T, \tag{34}$$

where k_Q and η_Q are the torsional stiffness and dissipation coefficient, respectively. $\Omega_T = (\boldsymbol{\Omega}_i - \boldsymbol{\Omega}_j)\cdot\mathbf{n}$ is the relative twisting rate, and $\xi_Q = \int_{t_0}^{t}\Omega_T(t)dt$ is the twisting displacement.

The energy equation to update the particle temperature under the varied temperature condition is given as follows:

$$mCp_s\frac{dT_p}{dt} = \oint\lambda\nabla T_f\cdot\mathbf{n}_b ds + Q_p, \tag{35}$$

where Cp_s is the heat capacity of the solid particle, T_p is the particle temperature, T_f is the fluid temperature, λ is the heat conductivity of fluid, $\mathbf{n}_b$ is the normal direction at the boundary, and Q_p is the heat source originated from the particle. It should be noted that the heat conduction

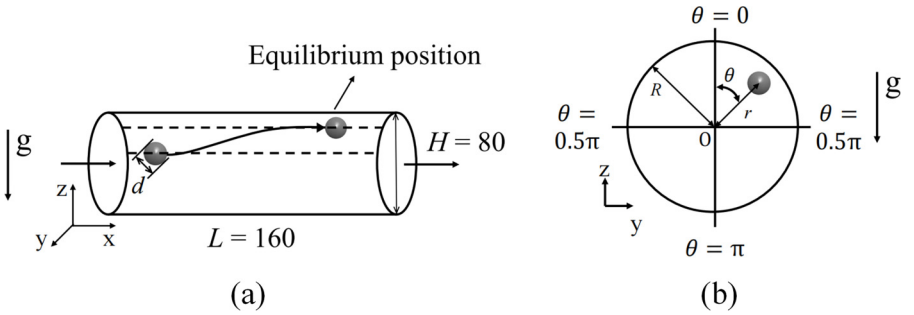

FIG. 2. Schematic of (a) geometry adopted in simulations and (b) particle position description in the *YZ* plane.

between particles is not considered due to its very tiny contribution. In addition, the Biot number of the particle is assumed to be small enough, so that the temperature gradient inside the particle is ignored.

III. PHYSICAL MODEL AND VALIDATION

In this section, we begin by introducing the physical model adopted in the present work, followed by a mesh validation. Then, two model validations are performed. The first one is the validation for fluid-solid coupling, while the second focuses on the thermal effect on particle movement.

The simulation geometry in the current study is shown in Fig. 2. The particle is initially placed in a cylindrical pipe full of Newtonian fluid. The initial velocities of both the fluid and the particle are set as zero. The fluid is driven by a pressure gradient implemented via a constant body force along the *X* direction, where periodic boundary conditions are imposed. The particle moves along the mainstream in the *X* direction, and migrates to a steady equilibrium position in the *YZ* plane from the initial position after a certain time. Particle position in the *YZ* plane is described using the polar coordinate which is symmetric about the *Z* axis. Throughout the migration process, the particle is influenced by multiple mechanisms including the wall repulsion, the Magnus force, the Saffman force, the lift force due to the curvature of the velocity, and the vertical buoyancy forces arising from thermal convection [40]. Note that, in the present work, we set the particle temperature lower than the fluid and wall temperatures, so that consequently the direction of thermal buoyancy is along the negative direction of the *Z* axis. The cylindrical wall is set as a no-slip boundary with constant temperature $T_w = 1$. Meanwhile, the initial fluid temperature is the same as the wall temperature $T_f = 1$ and the particle temperature is initially set as $T_p = 0$.

The particle inertial migration with thermal effect is controlled by several dimensionless numbers including the Reynolds number (Re), the Grashof number (Gr), the Richardson number (Ri), the Prandtl number (Pr), the heat capacity ratio of solid and fluid (Cp_r), and the density ratio between solid and fluid (ρ_r), which are given as

$$\mathrm{Re} = \frac{HU_f}{\upsilon_f}, \tag{36}$$

$$\mathrm{Gr} = \frac{g\beta(T_w - T_{p,0})H^3}{{\upsilon_f}^2}, \tag{37}$$

$$\mathrm{Ri} = \frac{\mathrm{Gr}}{\mathrm{Re}^2}, \tag{38}$$

$$\mathrm{Pr} = \frac{\upsilon_f}{\alpha}, \tag{39}$$

TABLE I. Parameters used in simulations in dimensionless lattice units.

Parameter	Value
Pipe length (L)	160
Pipe diameter (H)	80
Particle diameter (d)	8
Kinematic viscosity (ν_f)	0.05
Reynolds number (Re)	80, 160, 240
Grashof number (Gr)	10^0–10^6
Prandtl number (Pr)	0.7, 7, 70
Heat capacity ratio (Cp_r)	1–100
Particle temperature (T_p)	0
Wall temperature (T_w)	1

$$Cp_r = \frac{Cp_s}{Cp_f}, \tag{40}$$

$$\rho_r = \frac{\rho_s}{\rho_f}. \tag{41}$$

In the above equations, U_f is the velocity of fluid flow and Cp_f is the heat capacity of fluid. Re is used to scale the fluid inertial effect in this process. Gr is the parameter to characterize the relative strength of natural convection to buoyancy force. Ri is the combination of Gr and Re, which represents the importance of natural convection with respect to forced convection.

Table I lists the simulation parameters employed in this work, which are in dimensionless lattice units. The corresponding key physical parameters are given as the pipe length 4×10^{-3} m, the kinematic viscosity $1 \times 10^{-6}\,\mathrm{m}^2/\mathrm{s}$, and the fluid density $1000\,\mathrm{kg/m}^3$, respectively. The ratio between particle size and pipe diameter d/H is fixed as 0.1 in this study. In addition, for simulations with a constant temperature difference between the particle and wall, Pr is fixed as 7. Note that Cp_r is only meaningful for varied particle temperature simulations. Therefore, for simulations with a constant particle temperature, Cp_r is regarded as infinity, which implies that the particle temperature does not change with time. Meanwhile, the particles in the current work are assumed to be neutrally buoyant, indicating that the density ratio between solid and fluid is $\rho_r = \rho_s/\rho_p = 1$.

A mesh validation is first conducted by varying the particle diameter, where d/H and d/L are fixed as 0.1 and 0.05, respectively. Other parameters including Re = 160, Gr = 160, and Pr = 7 are

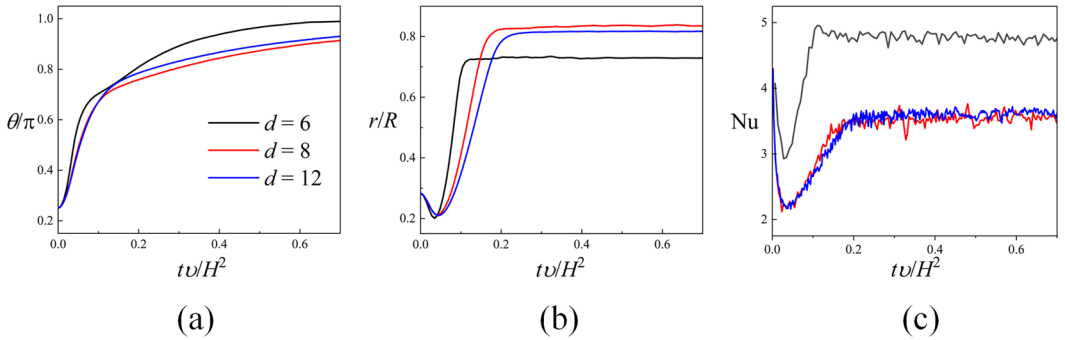

FIG. 3. Particle (a) circumferential position, (b) radial position, and (c) Nusselt number as a function of dimensionless time with different d.

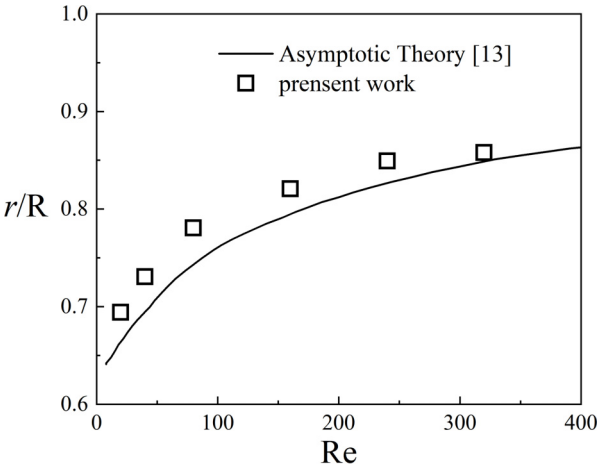

FIG. 4. Particle's radial equilibrium radial position for isothermal inertial migration.

fixed in the validation. The results are shown in Fig. 3, which demonstrate that $d = 8$ is a sufficient resolution to describe the particle behaviors in migration.

Then, two model validations are performed to verify the numerical method. In the first one, the inertial migration of a neutrally buoyant particle under isothermal condition is simulated, in order to confirm that the current model is capable of reproducing the well-known inertial migration phenomenon and predicting the particle's translation and rotation in fluid. The particle is initially released at $r = 0.2R$, and the geometry is the same as the model displayed in Fig. 2. Additionally, Re ranges from 20 to 320 and Pr is maintained as 7. The simulation results are shown in Fig. 4. It is clear that the current numerical model well captures the trend of equilibrium position with the increase of Re, compared with the theoretical result through a matched asymptotic expansion method [13].

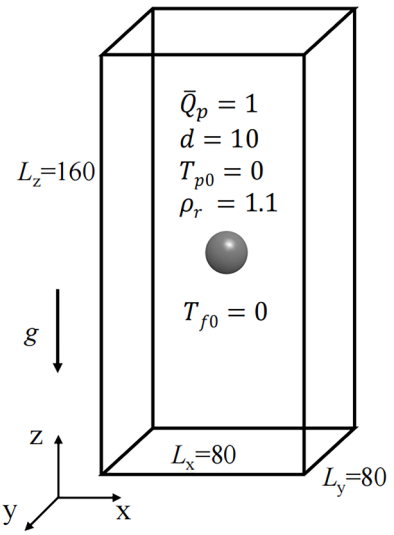

FIG. 5. Schematic of particle settling with constant heat source.

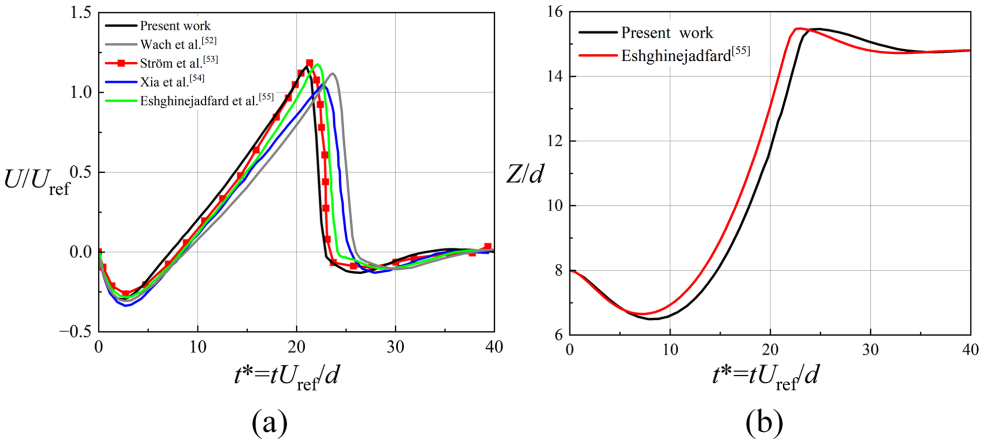

FIG. 6. Dimensionless particle (a) velocity and (b) position as a function of dimensionless time.

Figure 5 shows the physical model of the second validation in order to verify the particle movement under thermal convection. In this part, a spherical particle with an inner heat source settles in a rectangular enclosure chamber. The wall temperature is set as $T_w = 0$ at all the boundaries. Initially, the particle with the same temperature $T_p = 0$ as the fluid is released from the center of the box. $\mathrm{Re}_{\mathrm{ref}}$ and U_{ref} are used to describe the particle property, which are defined as

$$\mathrm{Re}_{\mathrm{ref}} = \frac{U_{\mathrm{ref}} d}{\nu_f}, \tag{42}$$

$$U_{\mathrm{ref}} = \sqrt{\frac{\pi d g(\rho_r - 1)}{2}}. \tag{43}$$

Furthermore, the particle temperature increases during the process due to the presence of inner heat source $\bar{Q}_p$, which is defined as

$$\bar{Q}_p = \frac{Q_p d}{\rho_f C p_f U_{\mathrm{ref}} (T_h - T_c)}, \tag{44}$$

where T_h and T_c are defined implicitly by Gr. $\bar{Q}_p = 1$ is maintained in this work. Due to the gravitational force, the particle firstly settles down along the negative direction of the Z axis. Then, with the increase of particle temperature, the buoyancy exerted on the particle increases and drives the particle to move upward along the positive direction of the Z axis. The dimensionless controlling parameters in the validation are $\mathrm{Re}_{\mathrm{ref}} = 40$, $\mathrm{Pr} = 0.7$, $\mathrm{Gr} = 1000$, $Cp_r = 1.0$, $\rho_r = 1.1$, and $\bar{Q}_p = 1.0$. As shown in Fig. 6, the dimensionless position and velocity of the particle in our simulation are compared with previous works, where good agreements are observed [52–55]. It is convincing that our current model is suitable for describing the thermal effect when the particle's temperature is different from the fluid's temperature.

IV. RESULTS AND DISCUSSION

A. Migration of a single particle with constant temperature

In this section, the migration of a single particle is firstly investigated. The Pr in this section are all maintained at 7. In Fig. 7, the particle trajectories in the YZ plane of different Gr with the same $\mathrm{Re} = 160$ and $y_0 = z_0 = 0.2R$ are displayed. The time interval between each point is 5000. It is shown that, when $\mathrm{Gr} = 1$, the migration process is similar to the isothermal migration, in which the particle directly migrates toward the wall and reaches an equilibrium position close to the wall. When Gr is 200 and 1000, the particle firstly migrates along the radial direction toward the wall

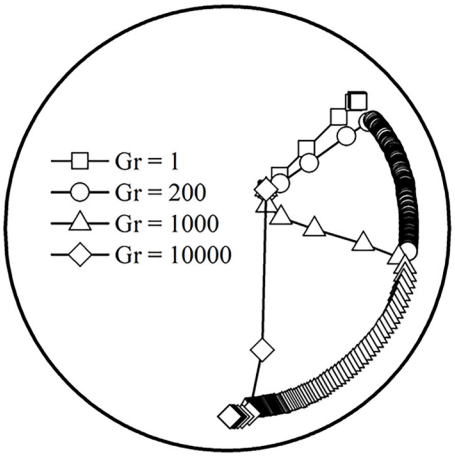

FIG. 7. The trajectory of particle migration in the *YZ* plane when Re = 160.

and reaches a radial equilibrium position. Then, due to the constant effect of buoyancy, the particle maintains the radial equilibrium position but moves downward to the bottom of the pipe, i.e., to a relatively larger circumferential position. However, as Gr reaches 10 000, the natural convection is more significant and the particle directly migrates toward the equilibrium position around the bottom of the pipe and approaches closer to the wall.

To further explore the equilibrium position of the migration, we conducted simulations with different Re, Gr, and initial positions. Four different initial positions are listed in Table II. We focus on the equilibrium circumferential and radial positions at the steady state, which do not change with time. The results of the particle positions are shown in Fig. 8.

According to Fig. 8(a), it is evident that the circumferential equilibrium position is determined by Ri and all data collapse to a single curve for a specific initial position, indicating that Ri is appropriate for correlating particle equilibrium circumferential positions. Consistent trends are observed for different initial positions, where θ_{eq} increases with Ri. In addition, when Ri exceeds 10^{-1}, all particles reach the bottom of the pipe with $\theta_{eq} = \pi$. Therefore, three distinct zones can be identified based on different ranges of Ri. In the case of $\mathrm{Ri} < 10^{-3}$, the thermal effects are negligible, and the particles tend to migrate directly toward the wall without any change in the initial circumferential position, which is similar to the isothermal condition in that only inertial migration is observed. Therefore, the zone with $\mathrm{Ri} < 10^{-3}$ is defined as the inertial lift dominating zone. With the Ri range spanning from 10^{-3} to 10^{-1}, the buoyancy resulting from thermal convection becomes comparable to the inertial lift, thereby establishing a sensitive correlation between θ_{eq} and Ri. A transition zone is thus identified within the specific range of $10^{-3} < \mathrm{Ri} < 10^{-1}$, in which the particle equilibrium position moves toward the pipe bottom with an increase of Ri. Subsequently, when $\mathrm{Ri} > 10^{-1}$, all particles with different initial positions converge to the same circumferential equilibrium position at the bottom of the pipe since the buoyancy attains sufficient strength to

TABLE II. Dimensionless parameters of different particle initial position.

Parameter	A	B	C	D
y_0/R	0.200	0.200	0.600	0.200
z_0/R	0.200	−0.200	0.000	0.600
θ_0/π	0.250	0.750	0.500	0.102
r_0/R	0.283	0.283	0.800	0.632

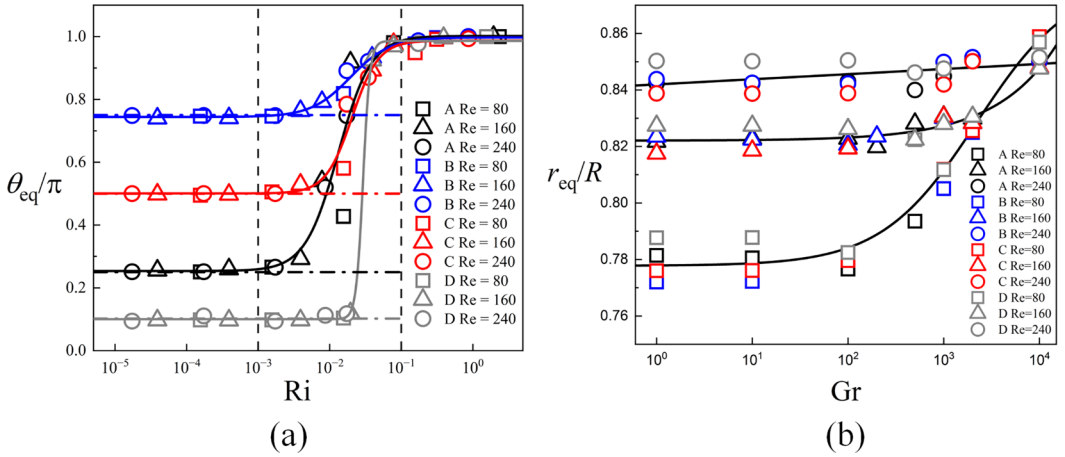

FIG. 8. The particle's (a) circumferential and (b) radial equilibrium positions as a function of Ri and Gr, respectively. The curves indicate the fitting lines of different initial position in panel (a) and different Re in panel (b). The vertical dashed lines divide the graph into three zones according to the range of Ri, while the horizontal dashed-dotted lines indicate the initial circumferential positions.

dominate over the inertial lift. Hence, for the range $\mathrm{Ri} > 10^{-1}$, the buoyancy dominating zone is defined.

Apart from the circumferential position, the radial equilibrium position of particles is also investigated, as shown in Fig. 8(b). In contrast to circumferential equilibrium positions, radial equilibrium positions, which are primarily influenced by Re, are found to be insensitive to initial positions. The effect of Gr is only evident when Re is small ($\mathrm{Re} = 80$) and $\mathrm{Gr} > 10^2$, which is due to the competitive relationship between inertial migration and thermal effect. As Gr increases, the buoyancy breaks the original radial force balance of inertial migration and gradually pushes the particle toward the bottom of the pipe, as depicted in Fig. 7. When Gr is quite large ($\mathrm{Gr} > 10^4$), where the particle is already focused around the bottom area, the buoyancy keeps pushing the particle toward the bottom wall, resulting in a smaller particle-wall distance, i.e., a larger radial position. A stronger wall repulsion force is thus produced to balance the buoyancy. For larger Reynolds numbers $\mathrm{Re} = 160$ and $\mathrm{Re} = 240$, the original radial equilibrium positions are larger due to the inertial effect, so that the effect of thermal effect, which leads to the increase of radial position, becomes much less obvious.

Except for particle equilibrium position, the intensity of particle heat transfer is also investigated, which is evaluated through the dimensionless Nusselt number that is defined as

$$\mathrm{Nu} = \frac{hd}{\lambda}, \tag{45}$$

where h is the convective heat transfer coefficient. In the simulation, Nu is calculated through the integration of the heat transfer at the lattice around the particle, which is expressed as

$$\mathrm{Nu} = \frac{\oint \mathrm{Nu}_{\mathrm{local}} ds}{\oint ds}, \tag{46}$$

$$\mathrm{Nu}_{\mathrm{local}} = \frac{d}{T_p - T_0} \frac{\partial T}{\partial n}. \tag{47}$$

For the inertial migration with a single particle when the particle initial position is case A in Table II, the variation of Nu with Gr is illustrated in Fig. 9. It can be seen that Nu increases insignificantly with Gr, and the increase is more significant when $\mathrm{Gr} > 10^2$. The trend of Nu increase aligns

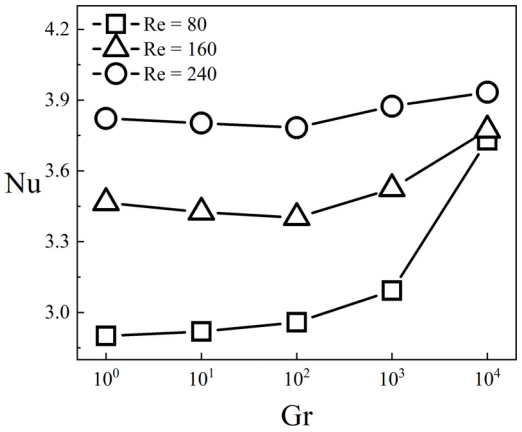

FIG. 9. The relation between Nu and Gr for the condition of a single particle with constant temperature.

with the r_{eq} increase with Gr in that the data variation is more obvious when Re = 80, in which the inertial effect is relatively weaker than other cases with larger Re. The observed increase of Nu is indeed correlated with the migration of the particle toward the wall and the concurrent increase in r_{eq}. As the particle position approaches the wall, the thermal convection around the particle is strengthened due to a more pronounced temperature difference in its closer proximity to the wall, which implies intensified thermal effects associated with the particle's migration toward the wall.

B. Migration of dilute suspension with constant temperature

The particle suspension with constant particle temperature is investigated in this section. The solid volume fraction of dilute suspension is maintained at 1% and the Prandtl number in this section is fixed as 7. Particles are initially distributed with random positions. The particle equilibrium position and temperature distribution of a flow field with different Gr when Re = 160 are illustrated in Fig. 10. Generally, the migration scenario of particle suspension migration is similar to that of the single particle. For instance, particles migrate directly toward the wall and are focused to an annulus between the center of the pipe and the wall when Gr is small ($Gr = 10^0$) as shown in Fig. 10(a). Notably, particle trains along the flow direction at the annulus are observed, which have been reported in numerous previous studies with isothermal conditions [19,56–58]. As Gr increases to 10^5, the equilibrium positions move downward and the particles tend to focus to the lower half annulus with the similar radial positions. Furthermore, with a larger Gr ($Gr = 5 \times 10^5$), particles are concentrated at the bottom of the pipe, aligning along the main flow direction.

The variations of the circumferential and radial equilibrium positions are illustrated in Fig. 11. To describe the particle positions in suspension, where the number of particles is n, the average equilibrium circumferential position $\theta_{av} = \frac{\sum_i^n \theta_i}{n}$ and radial position $r_{av} = \frac{\sum_i^n r_i}{n}$ are adopted, respectively. In terms of circumferential positions as shown in Fig. 11(a), the migration behavior can also be divided into three zones depending on the Ri range, which is similar tothe case of single-particle migration. When $Ri < 10^{-2}$, namely, in the inertial lift dominating migration zone, the θ_{av} is approximately 0.5π. This is attributed to the random particle distribution, which is not sensitive to the initial position of an individual particle. With an increase of the range of Ri, particles gradually migrate to the bottom of the pipe. However, it can be seen that the Ri range of the transition zone ($10^{-2} < Ri < 10^1$) is larger than the range of the single-particle condition ($10^{-3} < Ri < 10^{-1}$). This discrepancy is caused by the crowding of cold particles, where the temperature difference and natural convection arenot as significant as the single-particle situation, leading to a weakened buoyancy effect.

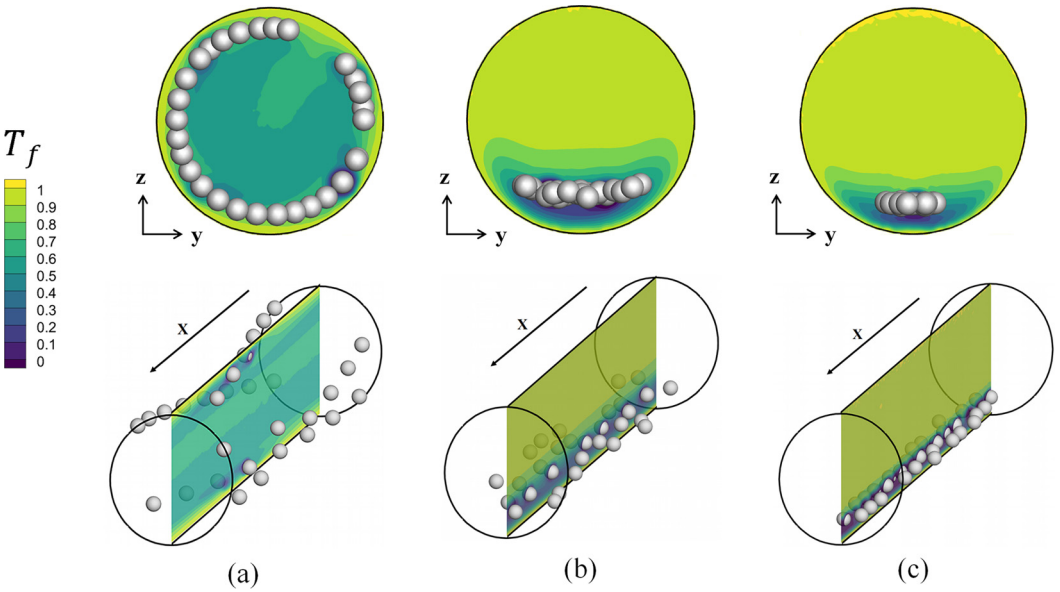

FIG. 10. Particle equilibrium positions and temperature distribution in the YZ plane when $X = 1$ and in the XZ plane when $Y = 40$ at (a) $\mathrm{Gr} = 10^0$, (b) $\mathrm{Gr} = 10^5$, and (c) $\mathrm{Gr} = 5 \times 10^5$ when $\mathrm{Re} = 160$, respectively.

As shown in Fig. 11(b), the average radial position of dilute suspension is significantly dependent on Re and almost does not change with Gr when $\mathrm{Gr} < 10^{-1}$. Subsequently, with the increase of Gr, r_{av} initially decreases and then increases, which shows a completely different nonmonotonic trend from the single-particle case as illustrated in Fig. 8(b). This is caused by the temperature disturbance due to the particle crowding effect, which does not exist for the singleparticle condition. As discussed in Sec. IV A, the particle migrates toward the pipe bottom with the increase of Gr. However, in the case of dilute suspension, particles gather together during the downward motion, where the local temperature field is disturbed due to the crowding particles and a low temperature zone is formed around the pipe bottom, as displayed in Fig. 10(b) with $\mathrm{Gr} = 10^5$. Consequently, the buoyancy force is weakened and the downward migration of some particles issuppressed because of

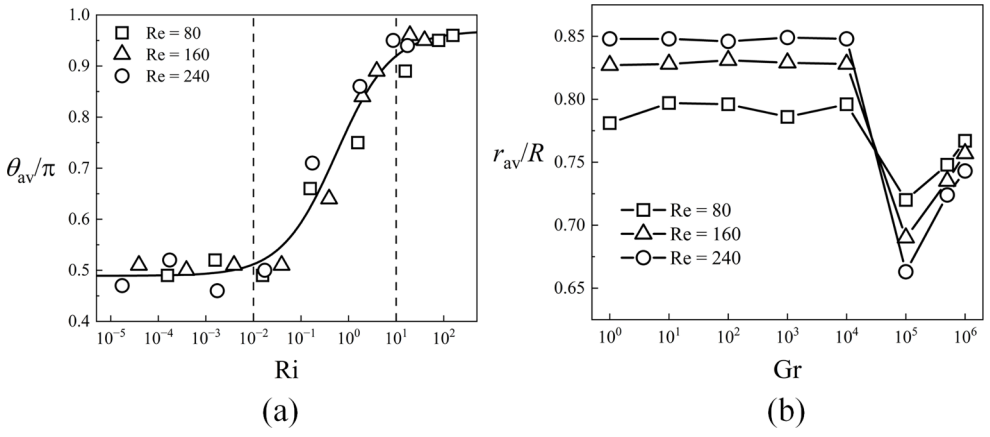

FIG. 11. The average particle (a) circumferential position as a function of Ri and (b) the average radial position as a function of Gr for particle suspension with constant temperature.

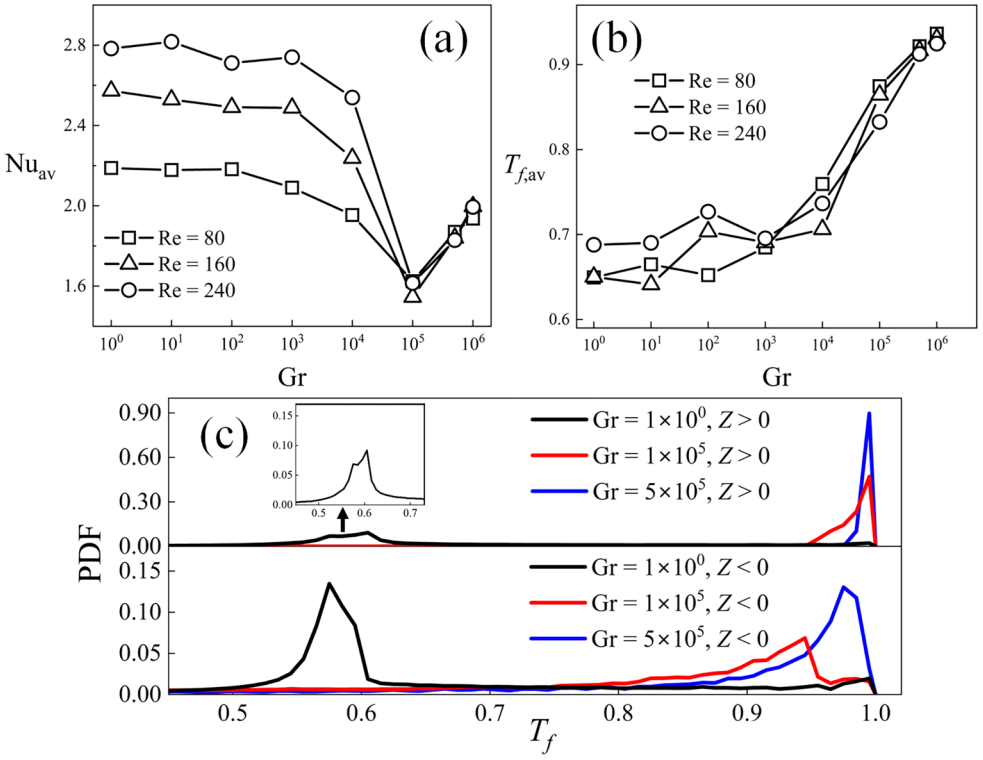

FIG. 12. (a) The average Nusselt number, (b) the average fluid temperature as a function of Gr, and (c) the probability density function of the fluid temperature.

the decrease in the effective temperature difference, which leads to a crescent particle distribution and the decrease of r_{av}. With the further increase of Gr ($\mathrm{Gr} > 10^5$), the thermal effect overwhelms the particle crowding effect during the migration and nearly all the particles are aligned close to the bottom wall, which leads to the increase of r_{av}.

To further elucidate the nonmonotonic variation of r_{av} and evaluate the influence of the particle crowding effect, several quantities with respect to the temperature field are characterized, which include the average Nusselt number of particles ($\mathrm{Nu}_{\mathrm{av}}$), the average fluid temperature ($T_{f,\mathrm{av}}$) as well as the probability density function (PDF) of the fluid temperature. The average Nusselt number is defined as $\mathrm{Nu}_{\mathrm{av}} = \frac{\sum_i^n \mathrm{Nu}}{n}$. The average fluid temperature is calculated as the mean temperature value of all the fluid lattices and the PDF represents the statistical property of the fluid temperature field. Figure 12(a) shows the $\mathrm{Nu}_{\mathrm{av}}$ as a function of Gr with different Re. When $\mathrm{Gr} < 10^3$, $\mathrm{Nu}_{\mathrm{av}}$ is almost irrelevant with Gr but mainly affected by Re. When $\mathrm{Gr} > 10^3$, the nonmonotonic trend, which is similar to the variation of r_{av} displayed in Fig. 11(b), is observed again. This similarity implies a close relation between r_{av} and $\mathrm{Nu}_{\mathrm{av}}$. As can be inferred from Eq. (47), $\mathrm{Nu}_{\mathrm{av}}$ is a direct description of the local temperature gradient around the particles. When $\mathrm{Gr} = 10^5$, the low-temperature zone due to the crowding particles suppresses the heat transfer, resulting in a decrease of $\mathrm{Nu}_{\mathrm{av}}$. Then, as $\mathrm{Gr} > 10^5$, the particles are more concentrated at the bottom of the pipe, leading to a much reduced low-temperature zone. Meanwhile, particle positions get closer to the pipe bottom wall with constant $T_w = 1$. Therefore, the temperature difference between the particles and fluid is increased again and $\mathrm{Nu}_{\mathrm{av}}$ increases correspondingly. It is noteworthy that, when $\mathrm{Gr} > 10^5$, the $\mathrm{Nu}_{\mathrm{av}}$ of different Re seems to collapse onto a single curve, suggesting that the fluid convection is not the primary effect but the conduction between the particle and the pipe wall dominates the heat transfer.

Figure 12(b) shows the variation of $T_{f,\mathrm{av}}$ as a function of Gr, where a monotonic increase is observed. The $T_{f,\mathrm{av}}$ represents the overall status of the fluid temperature field and can somehow reflect the degree of particle gathering. If the particles are evenly distributed in the pipe, the low-temperature zone created by the cold particles becomes large, which results in a lower value of $T_{f,\mathrm{av}}$. The monotonic increase of $T_{f,\mathrm{av}}$ indicates that the particles get much closer to each other as Gr increases. Moreover, the differences of $T_{f,\mathrm{av}}$ for different Re are tiny, implying that the particle gathering behavior is similar for different Re. However, $T_{f,\mathrm{av}}$ is not able to characterize the spatial location of particle gathering. Figure 12(c) further illustrates the PDFs of the fluid temperature in the upper and the lower half pipe, respectively, in order to demonstrate the nonuniformity of the temperature field. It is shown that when $\mathrm{Gr} = 1$, the PDFs are similar for both the upper and the lower pipe, where the peaks are around 0.6, suggesting a uniform temperature distribution in the entire region. As Gr is increased to 10^5, the peaks of the upper and lower pipes move to around 1 and 0.95, respectively. The nonuniform temperature distribution becomes evident, where the PDF for the lower pipe is much wider. Then, when $\mathrm{Gr} = 5 \times 10^5$, the PDF of the upper pipe is concentrated to a sharp peak around 1, and the peak of the lower pipe moves close to 1 again. In this stage, the temperature of the upper pipe is almost uniform at $T = 1$, while the temperature of the lower pipe is still in wider distribution but with larger value. The findings of Fig. 12(c) provide further evidence ofthe temperature disturbance due to the particle crowding effect, which strongly supports the above discussions and analyses.

C. Migration with varied particle temperature

In real applications, particle temperature variation influenced by the surrounding environment is also important. Therefore, we take the temperature variation of the particle into consideration and discuss its impact on the migration. Under this circumstance, the effects of two more important parameters, i.e., the relative heat capacity (Cp_r) and the Prandtl number (Pr), which determine the heating rate of the particle, are introduced. Since the particle temperature is varied, the buoyancy force exerted on the particle changes not only with the position, but also with time. As a result, the particle migration behavior becomes more complicated. In this section, the migrations of both singleparticle and dilute suspensions- are discussed. For singleparticle migration with varied particle temperature, the initial particle position is fixed with case A in Table II.

Figure 13 illustrates the typical particle trajectories as well as the particle temperature evolution, where Re is fixed as 160. The trajectories are similar tothose of the constant temperature condition. However, Cp_r and Pr play an important role on influencing the equilibrium position, since the buoyancy is related to the temperature difference between the particle and fluid. The particle temperature is varied and related to the heat transfer process, which is in turn influenced by the temperature difference and position. Observations from the trajectories indicate that, for smaller Pr and Cp_r, the particle temperature increases more rapidly, so that the migration is more prone to be the isothermal condition. Conversely, for larger Pr and Cp_r, the migration is affected by buoyancy for a longer time and it resembles the constant temperature difference condition.

Then, the equilibrium positions when $Cp_r = 100$ and $\mathrm{Pr} = 7$ are shown in Fig. 14. According to Fig. 14(a), similar to the situation of a single particle with constant temperature, three zones of the circumferential equilibrium position can be determined depending on the range of Ri. However, it can be seen that the transition zone is extended and the range is around $10^{-3} < \mathrm{Ri} < 0.2$. In addition, it is shown from Fig. 14(b) that the particle's radial equilibrium position is only determined by Re for the varied temperature process but is irrelevant with Gr, which is distinct from the constant temperature case. This is because the particle's temperature eventually becomes the same as the fluid's, and the migration always goes back to the isothermal case, where the radial equilibrium position only depends on Re.

Figure 15 further compares the particle equilibrium circumferential position with different Pr and Cp_r. The results are consistent with the analysis from the trajectory displayed in Fig. 13. With a decrease of Cp_r and Pr, the evolution of θ_{av} moves to the right, which results in the enlargement

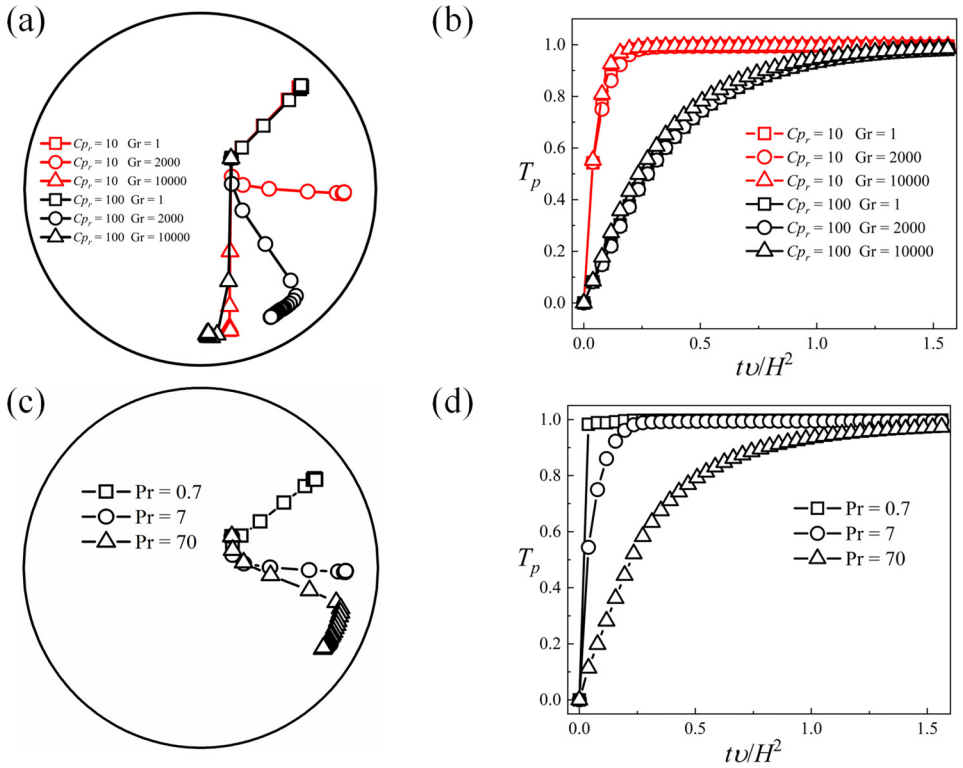

FIG. 13. Single particle's (a) migration trajectory and (b) temperature evolution with different Cp_r when Pr = 7, and (c) migration trajectory and (d) temperature evolution with different Pr when $Cp_r = 10$ and Gr = 2000.

of the transition zone and the requirement of a much larger Ri to induce the particle migration toward the pipe bottom. This is because it takes a shorter time for the particle to reach the boundary temperature for small Cp_r and Pr, only during which the buoyancy possesses an effect on the particle

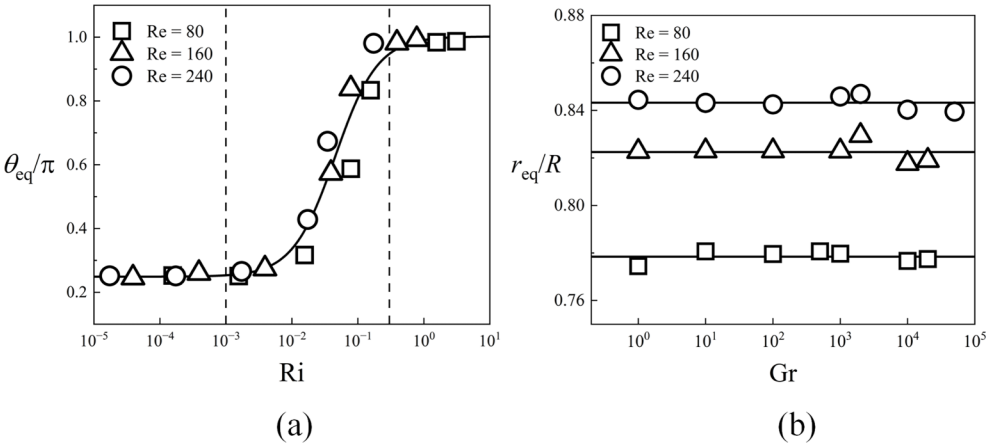

FIG. 14. (a) The circumferential and (b) radial equilibrium positions for a single particle with varied temperature when $Cp_r = 100$ and Pr = 7.

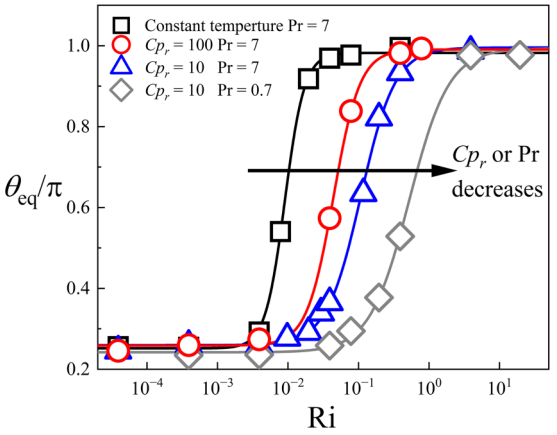

FIG. 15. The circumferential equilibrium position as a function of Ri for a single particle with varied temperature when Re = 160.

movement. To expedite the particle's movement toward the bottom of the pipe within a shorter time, a more substantial buoyancy effect is needed, corresponding to a larger Ri.

Then, the particle suspension with varied temperature is investigated. Particles are randomly distributed in the pipe with $T_p = 0$ initially. All simulations are set with $Cp_r = 10$, Pr = 7, and Re = 160. The θ_{av} of particles at different time points is recorded while r_{av} is not studied since it has been found that r_{av} is only related to Re for varied temperature conditions, as shown in Fig. 14(b). The evolution of θ_{av} with time is plotted in Fig. 16(a). For all simulation conditions, θ_{av} is initially around 0.5π due to the random distribution. It is shown that when Gr is small ($Gr < 1 \times 10^4$), the average circumferential positions do not change significantly with time, which is located around $\theta_{av} = 0.5\pi$ during the migration. However, when $Gr \geqslant 1 \times 10^5$, the evolution of θ_{av} undergoes three stages, which first rises rapidly, followed by a dropping down, and then gradually rises again to the equilibrium state. Firstly, the temperature difference between the particles and the fluid is large at the beginning of the migration, where the strong thermal effect quickly pushes the particles toward the pipe bottom, leading to the rapid increase of θ_{av}. Then, due to the increase of particle temperature, the temperature difference between the particle and the surrounding fluid becomes

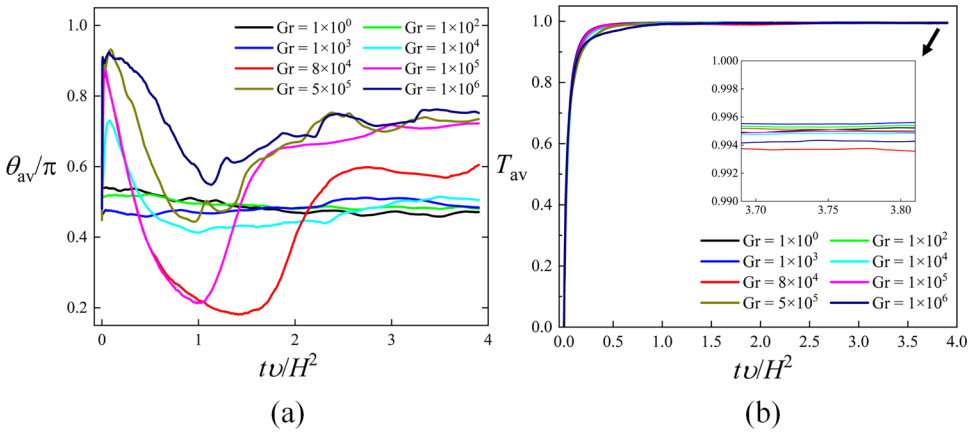

FIG. 16. Particle's average (a) circumferential equilibrium position and (b) temperature as a function of time when $Cp_r = 10$, Pr = 7, and Re = 160.

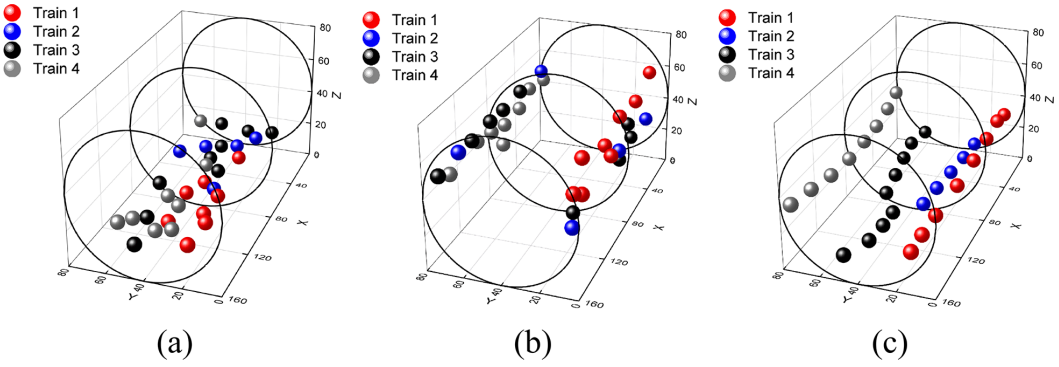

FIG. 17. Particle positions when (a) $tv/H^2 = 0.039$, (b) $tv/H^2 = 0.78$, and (c) $tv/H^2 = 3.9$ with the conditions of $Cp_r = 10$, Pr = 7, Re = 160, and Gr = 5×10^5.

smaller. Hence, the effect of thermal buoyancy is weakened and the particles crowded at the pipe bottom start to rearrange due to the fluid inertial effect. During this process, θ_{av} firstly decreases and then increases to the final steady state, where a slightly larger $\theta_{\text{av}} \approx 0.7\pi$ compared to the initial state is reached. For the condition $1 \times 10^4 < \text{Gr} < 1 \times 10^5$, the three stages are also observed, and θ_{av} is located between 0.5π and 0.7π. Figure 16(b) displays the time evolution of the average particle temperature. It can be seen that the particle temperature rises rapidly from the beginning of the migration and it almost reaches the equilibrium temperature when the particle rearrangement finishes at around $tv/H^2 = 1$. Furthermore, from the inset of Fig. 17(b), it is observed that there is still a tiny temperature difference $\Delta T \approx 0.005$ between the particles and the fluid due to the very low heat transfer rate approaching the steady state. This tiny temperature difference accounts for the slightly larger θ_{av} at the equil ibrium state when Gr $\geqslant 1 \times 10^5$.

Figure 17 shows a straightforward description of the evolution of particle positions with large Gr at different time points. Figure 17(a) denotes the particle crowding around the pipe bottom at the beginning, which corresponds to the first peak observed in Fig. 16(a) for Gr $\geqslant 1 \times 10^5$. Figure 17(b) illustrates the rearrangement of the particles during the second state, where the particles seem to be levitated and the θ_{av} decreases from the first peak value. Figure 17(c) shows the final equilibrium state, in which the particle temperature approaches the wall temperature and the entire system resembles the isothermal condition. It is interesting that the particle trains are observed again, as mentioned in Sec. IV B, which is believed to be evidence of the fluid inertial effect. To highlight the evolution of particle trains, different colors are utilized to identify the distinct trains. It is found that the particle trains are mixed at the beginning, start to take shape during the particle rearrangement, and eventually develop into the stabilized form at the equilibrium state.

V. CONCLUSIONS

In this study, the inertial migration of neutrally buoyant particles with thermal effect in a circular pipe is investigated by a coupled LBM-DEM numerical approach. Single-particle and dilute particle suspensions with both constant temperature and varied temperature conditions are investigated, respectively. Both the circumferential and the radial positions in terms of the cylindrical coordinates are adopted to describe the particle migration behavior. Furthermore, the heat transfer during the migration is evaluated via the dimensionless Nusselt number. The main findings of the current study are summarized as below.

(1) Generally, it is found that the particles tend to migrate toward the pipe bottom due to the thermal buoyancy when the fluid's temperature is higher than the particle's. However, the particle's circumferential equilibrium position is found to be controlled by the initial position and

the Richardson number, while the radial equilibrium position is determined by the Reynolds number as well as the Grashof number.

(2) For the migration of a single particle with constant temperature, three zones are identified to describe the circumferential equilibrium position θ in terms of Ri, including an inertial lift dominating zone with $\mathrm{Ri} < 10^{-3}$, a transition zone with $10^{-3} < \mathrm{Ri} < 10^{-1}$, and a buoyancy dominating zone with $\mathrm{Ri} > 10^{-1}$. For the radial equilibrium position r, it appears to increase with the increase of Gr. But the increment is only evident for a small Reynolds number, which is $\mathrm{Re} = 80$ in the current study. Meanwhile, the heat transfer rate, which is characterized by Nu, strongly depends on Re and increases insignificantly when $\mathrm{Gr} > 10^3$.

(3) For the migration of a dilute suspension with constant temperature, the evolution of the average circumferential equilibrium position θ_{av} is similar to the single-particle situation except for an enlarged transition zone. However, the average radial equilibrium position r_{av} and Nusselt number $\mathrm{Nu}_{\mathrm{av}}$ perform a nonmonotonic variation as a function of Gr, which is due to the temperature disturbance caused by the particle crowding in the near wall area around the pipe bottom.

(4) For a single particle with varied temperature, the heat capacity ratio Cp_r and the Prandtl number Pr determine the migration behavior, which exhibits the characteristic of isothermal condition for larger Cp_r and Pr but resembles the constant temperature condition for small Cp_r and Pr. Additionally, the transition zone of the evolution of θ is enlarged with the decrease of Cp_r and Pr. The radial equilibrium position r is found to be only determined by Re but irrelevant with Gr.

(5) For the migration of particle suspension with varied temperature, the particles' average circumferential positions evidently do not change with time and are located around $\theta_{\mathrm{av}} = 0.5\pi$ when Gr is lower than a threshold value and other parameters are fixed, which is $\mathrm{Gr} = 10^5$ and $Cp_r = 100$, $\mathrm{Pr} = 7$, and $\mathrm{Re} = 160$ in the current study. Once $\mathrm{Gr} \geqslant 10^5$, a three-stage fluctuation is observed and the final $\theta_{\mathrm{eq,av}}$ is discovered to be slightly larger than 0.5π. Moreover, the formation of particle trains is also revealed in the migration with thermal effect, which is only reported in previous works on isothermal migration.

ACKNOWLEDGMENTS

This work is supported by the National Natural Science Foundation of China (Grants No. 52106214 and No. 32100096), the IPE Project for Frontier Basic Research (Grant No. QYJC-2022–002), and the Research Fund of State Key Laboratory of Mesoscience and Engineering (MESO-23-A04).

[1] S. Kuang, M. Zhou, and A. Yu, CFD-DEM modelling and simulation of pneumatic conveying: A review, Powder Technol. **365**, 186 (2020).

[2] J. M. Martel and M. Toner, Inertial focusing in microfluidics, Annu. Rev. Biomed. Eng. **16**, 371 (2014).

[3] G. Segré and A. Silberberg, Radial particle displacements in Poiseuille flow of suspensions, Nature (London) **189**, 209 (1961).

[4] D. Di Carlo, Inertial microfluidics, Lab Chip **9**, 3038 (2009).

[5] R. N. Valani, B. Harding, and Y. M. Stokes, Utilizing bifurcations to separate particles in spiral inertial microfluidics, Phys. Fluids **35**, 011703 (2023).

[6] S. Razavi Bazaz, Zigzag microchannel for rigid inertial separation and enrichment (Z-RISE) of cells and particles, Lab Chip **22**, 4093 (2022).

[7] H. Cha, H. Fallahi, Y. Dai, S. Yadav, S. Hettiarachchi, A. McNamee, H. An, N. Xiang, N.-T. Nguyen, and J. Zhang, Tuning particle inertial separation in sinusoidal channels by embedding periodic obstacle microstructures, Lab Chip **22**, 2789 (2022).

[8] G. Esposito, S. Romano, M. A. Hulsen, G. D'Avino, and M. M. Villone, Numerical simulations of cell sorting through inertial microfluidics, Phys. Fluids **34**, 072009 (2022).

[9] E. J. Hinch and J. A. Schonberg, Inertial migration of a sphere in Poiseuille flow, J. Fluid Mech. **203**, 517 (1989).
[10] E. S. Asmolov, The inertial lift on a spherical particle in a plane Poiseuille flow at large channel Reynolds number, J. Fluid Mech. **381**, 63 (1999).
[11] É. Guazzelli, J.-P. Matas, and J. F. Morris, Lateral force on a rigid sphere in large-inertia laminar pipe flow, J. Fluid Mech. **621**, 59 (2009).
[12] M. Han, C. Kim, M. Kim, and S. Lee, Particle migration in tube flow of suspensions, J. Rheol. **43**, 1157 (1999).
[13] J.-P. Matas, J. F. Morris, and É. Guazzelli, Inertial migration of rigid spherical particles in Poiseuille flow, J. Fluid Mech. **515**, 171 (2004).
[14] D. Di Carlo, J. F. Edd, K. J. Humphry, H. A. Stone, and M. Toner, Particle segregation and dynamics in confined flows, Phys. Rev. Lett. **102**, 094503 (2009).
[15] X. Shao, Z. Yu, and B. Sun, Inertial migration of spherical particles in circular Poiseuille flow at moderately high Reynolds numbers, Phys. Fluids **20**, 103307 (2008).
[16] D.-K. Sun and Z. Bo, Numerical simulation of hydrodynamic focusing of particles in straight channel flows with the immersed boundary-lattice Boltzmann method, Int. J. Heat Mass Transfer **80**, 139 (2015).
[17] B. Chun and A. J. C. Ladd, Inertial migration of neutrally buoyant particles in a square duct: An investigation of multiple equilibrium positions, Phys. Fluids **18**, 031704 (2006).
[18] W. Liu and C.-Y. Wu, Analysis of inertial migration of neutrally buoyant particle suspensions in a planar Poiseuille flow with a coupled lattice Boltzmann method-discrete element method, Phys. Fluids **31**, 063301 (2019).
[19] T. Hafemann and J. Fröhlich, Inertial migration of non-spherical particles in straight microfluidic channels, Phys. Fluids **35**, 013328 (2023).
[20] X. Hu, J. Lin, P. Lin, and Z. Zhu, Rigid spheroid migration in square channel flow of power-law fluids, Int. J. Mech. Sci. **247**, 108194 (2023).
[21] G. Lauricella, J. Zhou, Q. Luan, I. Papautsky, and Z. Peng, Computational study of inertial migration of prolate particles in a straight rectangular channel, Phys. Fluids **34**, 082021 (2022).
[22] T. Krüger and B. Owen, Numerical investigation of the formation and stability of homogeneous pairs of soft particles in inertial microfluidics, J. Fluid Mech. **937**, A4 (2022).
[23] L. Huang, J. Lin, R. Wang, and C. Shao, Inertial migration of soft particles initially evenly spaced along the flow direction in a channel, Phys. Fluids **34**, 103308 (2022).
[24] T. Omori, M. Sugihara-Seki, N. Takeishi, S. Wada, H. Yamashita, and N. Yokoyama, Inertial migration of red blood cells under a Newtonian fluid in a circular channel, J. Fluid Mech. **952**, A35 (2022).
[25] H. Zhang and S. Li, DEM simulation of wet granular-fluid flows in spouted beds: Numerical studies and experimental verifications, Powder Technol. **318**, 337 (2017).
[26] S. Chen, S. Li, and J. S. Marshall, Exponential scaling in early-stage agglomeration of adhesive particles in turbulence, Phys. Rev. Fluids **4**, 024304 (2019).
[27] S. Chen, S. Li, and X. Ruan, Effect of long-range Coulomb repulsion on adhesive particle agglomeration in homogeneous isotropic turbulence, J. Fluid Mech. **915**, A131 (2021).
[28] S. Chen, W. Liu, and S. Li, A fast adhesive discrete element method for random packings of fine particles, Chem. Eng. Sci. **193**, 336 (2019).
[29] Z. Fang, Y. Zhang, M. Wei, S. Zhao, X. Wu, and L. Sun, A numerical study on adhesive collision between a micro-sized particle and a wall, Powder Technol. **360**, 769 (2020).
[30] R. Wang, S. Sun, W. Wang, and Z. Zhu, Investigation on the thermophoretic sorting for submicroparticles in a sorter with expansion-contraction microchannel, Int. J. Heat Mass Transfer **133**, 912 (2019).
[31] R.-Y. Dong, Y. Zhou, C. Yang, and B.-Y. Cao, Translational thermophoresis and rotational movement of peanut-like colloids under temperature gradient, Microfluid. Nanofluid. **19**, 805 (2015).
[32] T. Dbouk and S. A. Bahrani, Modeling of buoyancy-driven thermal convection in immersed granular beds, Int. J. Multiphase Flow **134**, 103471 (2021).
[33] V. Kumar, Vikash, and K. D. P. Nigam, Multiphase fluid flow and heat transfer characteristics in microchannels, Chem. Eng. Sci. **169**, 34 (2017).

[34] L. Biferale, P. Perlekar, M. Sbragaglia, and F. Toschi, Convection in multiphase fluid flows using lattice Boltzmann methods, Phys. Rev. Lett. **108**, 104502 (2012).
[35] Z. Yu, X. Shao, and A. Wachs, A fictitious domain method for particulate flows with heat transfer, J. Comput. Phys. **217**, 424 (2006).
[36] Z.-G. Feng and E. E. Michaelides, Heat transfer in particulate flows with direct numerical simulation (DNS), Int. J. Heat Mass Transfer **52**, 777 (2009).
[37] H. Gan, J. Chang, J. J. Feng, and H. H. Hu, Direct numerical simulation of the sedimentation of solid particles with thermal convection, J. Fluid Mech. **481**, 385 (2003).
[38] B. Yang, S. Chen, C. Cao, Z. Liu, and C. Zheng, Lattice Boltzmann simulation of two cold particles settling in Newtonian fluid with thermal convection, Int. J. Heat Mass Transfer **93**, 477 (2016).
[39] Z. Hashemi, O. Abouali, and R. Kamali, Three dimensional thermal lattice Boltzmann simulation of heating/cooling spheres falling in a Newtonian liquid, Int. J. Therm. Sci. **82**, 23 (2014).
[40] J. Hu and Z. Guo, A numerical study on the migration of a neutrally buoyant particle in a Poiseuille flow with thermal convection, Int. J. Heat Mass Transfer **108**, 2158 (2017).
[41] W. Liu and C.-Y. Wu, Inertial migration of a neutrally buoyant circular particle in a planar Poiseuille flow with thermal fluids, Phys. Fluids **33**, 063315 (2021).
[42] W. Liu and C.-Y. Wu, Inertial migration of a non-neutrally buoyant particle in a linear shear flow with thermal convection, Phys. Rev. Fluids **6**, 064306 (2021).
[43] W. Liu and C.-Y. Wu, Lateral migration of a neutrally buoyant particle in Couette flow with thermal convection, Int. J. Multiphase Flow **138**, 103612 (2021).
[44] Z. Guo, B. Shi, and N. Wang, Lattice BGK model for incompressible Navier–Stokes equation, J. Comput. Phys. **165**, 288 (2000).
[45] E. P. Gross and M. Krook, Model for collision processes in gases: Small-amplitude oscillations of charged two-component systems, Phys. Rev. **102**, 593 (1956).
[46] Z. Guo, B. Shi, and C. Zheng, A coupled lattice BGK model for the Boussinesq equations, Int. J. Numer. Methods Fluids **39**, 325 (2002).
[47] Z. Guo, C. Zheng, and B. Shi, Discrete lattice effects on the forcing term in the lattice Boltzmann method, Phys. Rev. E **65**, 046308 (2002).
[48] C. Peng, Y. Teng, B. Hwang, Z. Guo, and L.-P. Wang, Implementation issues and benchmarking of lattice Boltzmann method for moving rigid particle simulations in a viscous flow, Comput. Math. Appl. **72**, 349 (2016).
[49] D. Yu, R. Mei, L.-S. Luo, and W. Shyy, Viscous flow computations with the method of lattice Boltzmann equation, Prog. Aerosp. Sci. **39**, 329 (2003).
[50] T. Zhang, B. Shi, Z. Guo, Z. Chai, and J. Lu, General bounce-back scheme for concentration boundary condition in the lattice-Boltzmann method, Phys. Rev. E **85**, 016701 (2012).
[51] P. Costa, B. J. Boersma, J. Westerweel, and W.-P. Breugem, Collision model for fully resolved simulations of flows laden with finite-size particles, Phys. Rev. E **92**, 053012 (2015).
[52] A. Wachs, Rising of 3D catalyst particles in a natural convection dominated flow by a parallel DNS method, Comput. Chem. Eng. **35**, 2169 (2011).
[53] H. Ström and S. Sasic, A multiphase DNS approach for handling solid particles motion with heat transfer, Int. J. Multiphase Flow **53**, 75 (2013).
[54] J. Xia, K. Luo, and J. Fan, Simulating heat transfer from moving rigid bodies using high-order ghost-cell based immersed-boundary method, Int. J. Heat Mass Transfer **89**, 856 (2015).
[55] A. Eshghinejadfard and D. Thévenin, Numerical simulation of heat transfer in particulate flows using a thermal immersed boundary lattice Boltzmann method, Int. J. Heat Fluid Flow **60**, 31 (2016).
[56] J.-P. Matas, V. Glezer, É. Guazzelli, and J. F. Morris, Trains of particles in finite-Reynolds-number pipe flow, Phys. Fluids **16**, 4192 (2004).
[57] D. Di Carlo, H. Haddadi, and S. Kahkeshani, Preferred interparticle spacings in trains of particles in inertial microchannel flows, J. Fluid Mech. **786**, R3 (2016).
[58] Z. Pan, R. Zhang, C. Yuan, and H. Wu, Direct measurement of microscale flow structures induced by inertial focusing of single particle and particle trains in a confined microchannel, Phys. Fluids **30**, 102005 (2018).